

# Litho-Structural Mapping via Machine Learning and Geodata on Remotely Sensed Data in the Tharaka-Kanzungo, Kitui-Kenya

Jerald Odek<sup>1, 2\*</sup> Mark Boitt<sup>2</sup> Kuria Thiong'o<sup>2</sup> Patrick Kariuki<sup>3</sup>
1. Department of Geology and Meteorology, South Eastern Kenya University, Kitui, Kenya
2. Institute of Geomatics, GIS and Remote Sensing, Dedan Kimathi University of Technology, Nyeri, Kenya;
3. Institute of Geothermal Training and Research, Dedan Kimathi University of Technology, Nyeri, Kenya;

\* E-mail of the corresponding author: jeryodek@gmail.com

#### **Abstract**

Litho-structural mapping is critical for resource exploration and hazard assessment, supporting economic development. This study applies Planetscope and ALOS Palser DEM data to conduct lithological and structural mapping in the Tharaka-Kanzungo region of Kenya's Northern Kitui County. The approach integrates support vector machine classification with manual (shaded relief) and automatic (PC Line module) lineament extraction. Planetscope's high spatial resolution enabled effective rock unit discrimination, while ALOS Palser DEM data enhanced linear-structural analysis. SVM classification achieved 76.24% accuracy and a kappa of 70%, successfully identifying lithologies such as granitoid gneiss, semi-pelitic, calc-silicate, sillimanite-biotite, hornblendite, and crystalline limestone. Comparative results showed automatic methods detected more, shorter lineaments sensitive to texture and vegetation, whereas manual extraction captured fewer, longer, and distinct orientations. Stereographic projections further revealed tectonic features including shear foliations and lineations, aiding tectonic interpretation. The dominant NE-SW and NW-SE trends indicate structural influence on fluid pathways and potential mining zones. The integration of remote sensing techniques with ground-based validation produced a high-accuracy geological map, consistent with existing data. This approach demonstrates strong potential for updating maps and guiding mineral exploration in remote or inaccessible regions.

**Keywords:** Litho-structural mapping; Tharaka-Kanzungo; Machine learning; Lineaments extraction; Remote Sensing; Planetscope; Support vector machine; ALOS Palser DEM

**DOI:** 10.7176/JEES/15-5-02

Publication date: October 31st 2025

# 1. Introduction

Geological mapping is essential for exploring mineral, oil, and water resources and assessing natural hazards, contributing directly to economic development (Bachri, I. et al., 2020). A key phase in mineral exploration is identifying geological characteristics linked to target mineralization via the analysis geological maps, which display elements including lithological formations, alteration domains, structural features, and diagnostic minerals (Shirmard et al., 2022). Satellite imagery provides efficient, economically viable lithological classification, overcoming labor-intensive traditional field methods, especially in remote areas (Q. Zhang et al., 2025). When it comes to mineral exploration, the stakes are high, and having accurate geoscience data, like geological structures and mineral potential maps, is essential for making informed decisions and discovering new resources (Maghsoudi & Nader Fathianpour., 2016).

The Tharaka-Kanzungo region, nestled within Sub-area II of the Eastern Mozambique Belt System, is made up of a fascinating mix of granitoid, quartzites, biotite, and hornblende gneisses (Crowther, 1957; Dodson, 1955; Githenya et. al., 2021; Nyamai C., 1999). These rock types have gone through quite a bit of deformation due to regional tectonics and intense metamorphic processes, which have a significant function within the creation of valuable mineral deposits. Mozambique Belt rock units are generally thought to be metasedimentary in nature, and they have certainly piqued the interest of geologists over the years (Crowther, 1957; Dodson, 1955). Lineaments, closely linked to faults and fractures, are key indicators of subsurface mineral deposits. Their detection enhances mineral prospecting, making remote sensing a vital tool in geological mapping and exploration (Choudhury et al., 2025).

Mineral exploration in Kenya has largely relied on ground-based mapping, which is labor-intensive, costly, and limited in remote areas. Sentinel-2 imagery has proven effective for high-resolution lithological and structural characterization (Cardoso, F. et al., 2019). Although image-processing techniques like band ratios, band



combinations, and PCA aid in exploration, spectral confusion, particularly with agricultural land, can affect accuracy (Cardoso-Fernandes et al., 2020). Integrating fieldwork with supervised machine learning classifiers such as SVM, known for its high accuracy, enhances the precision for lithological characterization and minera exploration (Hu et al., 2018).

High-resolution PlanetScope imagery, generated from over 200 Dove satellites with up to eight bands and 3m resolution, allows daily revisits (Planet L., 2018), enhancing spectral and temporal analysis for geological mapping (Roy et al., 2021). Additionally, Alos Palser DEM with 12.5m resolution (Alaska Facility Services) supports topographic analysis and lineament detection (Ombiro, et al., 2021; Zafaty et al., 2023). Combining PALSER and ASTER datasets improves geological interpretation, providing more accurate and detailed mapping results than using either dataset alone. These advancements have significantly strengthened remote sensing applications in geology (Pour & Hashim, 2014). Geological mapping remains challenging in structurally complex regions with outdated maps, leading to misinterpretations. In Kenya, underexploited mineral reserves persist due to limited funding and inadequate technological infrastructure, despite growing global mineral demand (Karuku, 2008; Kiptarus J. et al., 2015; Kugeria P. M., 2022).

The Tharaka-Kanzungo area holds significant untapped mineral potential, but outdated geological and mineral potential maps from the 1950s hinder modern exploration (Crowther, 1957; Dodson, 1955). Although machine learning has improved geological data extraction, selecting suitable satellite-derived data for advanced lithostructural mapping remains challenging. Integration of remote sensing with traditional methods is promising, but single-source data limits accuracy. GIS/remote sensing offer initial insights but cannot fully replace field surveys for comprehensive mineral exploration. Instead, these technologies help narrow down target areas for more indepth geological, geochemical, and geophysical assessments on the ground, ultimately aiding in the selection of the best drilling sites (Chepchumba et al., 2019; Maarifa et al., 2024)

Integrating Gis and remote sensing with field investigations and conventional exploration techniques is essential for accurate geological mapping. This multidisciplinary approach enables more informed, cost-effective decision-making in resource evaluation and development. No prior studies have focused on remotely sensed Litho-structural data in Tharaka-Kanzungo, despite clear hydrothermal alteration suggesting mineralization, leaving a critical gap in geological understanding (Crowther, 1957; Dodson, 1955; Karuku, 2008; Kiptarus J. et al., 2015). This study updates the Litho-structural mineralization map of Tharaka-Kanzungo using enhanced PlanetScope imagery and SVM classification. It evaluates manual and automatic lineament extraction from Alos Palser DEM and validates results through field surveys and geological records.

## 2. Geological Setting of the Study Area

Tharaka-Kanzungo covers approximately 160 km² section, within the Eastern Mozambique Belt rocks in Kitui North, between latitudes 0°18′S–0°27′S and longitudes 38°00′E–38°05′E (Fig. 1). Crowther, 1957 and others described Tharaka-Kanzungo as composed mainly of granitoid gneiss, quartzites, gneisses, and metamorphosed sediments, with anorthositic rocks extensively boudinaged in later tectonic phases (Dodson, 1955; Nyamai et al., 1993; Nyamai C., 1999).

Kenya's Mozambique Belt experienced three tectonic phases, with dominant NNW-SSE to NW-SE trends, revealing early Earth history (Fig. 1) (Waswa, 2015; Nyamai, 1999). The geological features within the research region, comprise of intricate overlapping minor and major structures, as delineated by (Crowther, 1957). These structures comprise faults, folds, and linear features. The area is characterized by prevalent dip faults, predominantly oriented from northwest to southeast (Crowther, 1957). Faults in Tharaka-Kanzungo can be recognized through the linear vegetation arrangement, sudden altitude shifts, and the linear alignment observed in the area's drainage system (Crowther, 1957). Research by (Nyamai C., 1999) in neighboring areas, geology reveals diverse fold types. N-S mafic bodies within the Mozambique belt correlate with granulite facies mineralogical distribution (Nyamai C., 1999).



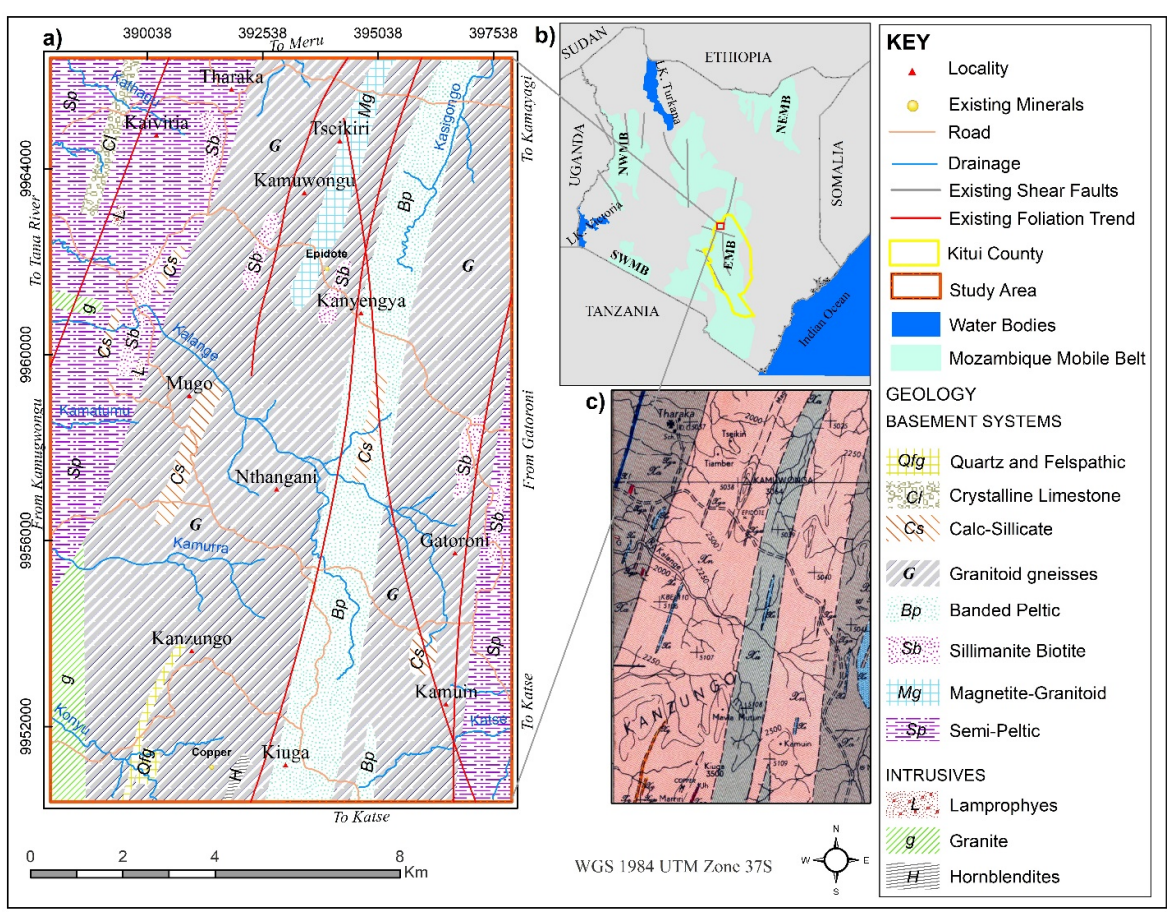


**Fig. 1:** a) Modified geological map illustrating various lithological units, b) Kenya and Kitui county map and c) Existing geological and structural map (Crowther, 1957; Dodson, 1955).

## 3. Material and Methods

#### 3.1 Datasets

This study utilized Planetscope imagery for lithological classification and ALOS/PALSAR DEM for lineament extraction in the Tharaka-Kanzungo area, with data accessed from Planet and Alaska Facility Services. A cloud-free, 3m high-resolution PlanetScope image (September 2024, dry season) with four bands (0.45-0.86 µm) (Table 1) was selected to minimize atmospheric disturbances and enhance surface visibility for lithological feature classification. Topographic and regional geological maps (Survey of Kenya/State Dpt. of Mining), administrative shapefiles (Geofabric, ICPAC Portal), and field survey data complemented this (Table 2).

For structural analysis, a Level 1.5 ALOS/PALSAR DEM image (September 2024, FBS mode, L-HH polarization, 12.5m resolution) was used (Table 1). Developed by METI and JAXA, ALOS/PALSAR is ideal for mapping complex topography and structural orietations (Northeast–Southwest, North–South, Northwest–Southeast). Data processing and analysis were performed using PCI Geomatica Banff and ArcGIS platforms. Field investigations involved GPS for coordinates, a compass for orientation measurements, a digital camera for photographs, and a geological hammer for rock sample collection, along with labeling and storage supplies (Table 2).



**Table 1:** Characteristics of PlanetScope imagery and PALSAR, functioning as an L-band Synthetic Aperture Radar (SAR) sensor with four polarization modes: HH (horizontal transmit/receive), HV (horizontal transmit, vertical receive), VV (vertical transmit/receive), and VH (vertical transmit, horizontal receive) (Planet L., 2018; Bannari et al., 2016; Shirmard et al., 2021).

PlanetScope		ALOS PA	LSER				
		Sensor	Mode	Polarization	Resolution (m)	S.W (km)	Incident angle
Inclination	98°	PALSER	Fine	(VV / (HH + HV) or (VV + VH))	10	70	8-60°
Orbit height	475 km		Scan Sar	HH or VV polarization	100	250-350	18-43°
Area coverage	16.4 km by 24.6 km		Polarimetric	Combined HH, HV, VH, and VV polarizations	30	30	8-30°
Orbit	Sun-synchronous						
Spatial resolution	3m by 3 m						
Temporal resolution	Daily (since 2017)						
Radiometric resolution	16 bit						
Band and wavelength (μm)	Band 1 (Blue) 0.45 - 0.51 Band 2 (Green) 0.50 - 0.59 Band 3 (Red) 0.59 - 0.67 Band 4 (NIR) 0.78 - 0.86						
Equatorial crossing time	9.30-11.30 local time						



Table 2: Summary of the datasets required.

ID	Data Specification		Application	Source		
1	PlanetScope	GeoTIFF, 3m Spatial resolution, WGS 1984 UTM 37s, November 2024	Lithological Classification	Planet Lab		
2	ALOS Palser DEM	GeoTIFF, 12.5m Spatial resolution, WGS 1984 UTM 37s, September 2024	Linear-Structural Extraction	Alaska Facility Services		
3	Administrative boundaries	Shapefile, WGS 1984, GCS.	Area of Study, Transportation, drainage pattern, and localities.	Geofabric, ICPAC Portal.		
4	Toposheet /Aerial	JPEG, WGS 1984, GCS,	Thematic layer, Planning,	Survey of Kenya/State		
	Photo, Existing geological Survey Map, GPS	1: 125,000, 1: 50,000, Garmin	orientation, Locating mineral/rock contacts, Geological Units,	Dpt. of Mining, South Eastern Kenya University, Geology and Met. Dpt.		
5	Qgis 3.4, ArcMap/ArcGIS Pro, PCI Geomatica, and Rockworks 16	N/A	Rose diagram, automatic lineament-structures extractions, Digital image processing and analysis.	https://qgis.org/, Esri, http://www.pcigeomatics. com/		
6	Hand Lenses 10x,	N/A	Small mineral crystals and	South Eastern Kenya		
	Measure, Shovel, Geological (hammer, Compasses, Tape measure)		structures in rocks, Length, and height of Rock information, Splitting and breaking rocks, orientation of Geologic structures, Strike and Dip.	University, Geology and Met. Dpt.		

Satellite image analysis from Planetscope (Fig. 2) involved systematic data preprocessing and classification. These procedures are categorized into two main phases: preprocessing and processing. The processing phase further differentiates between lithological classification and lineament-structural extraction, as detailed in the subsequent sections.



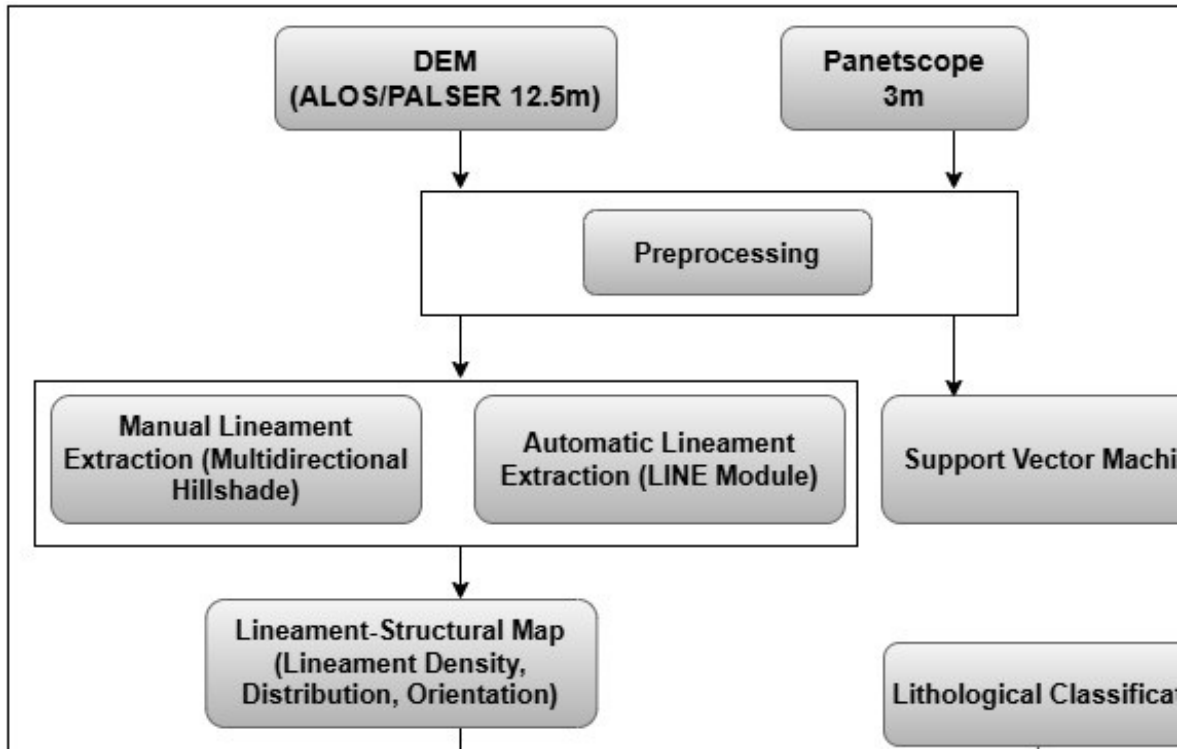


Fig. 2: Methodological flowchart adopted in this study

# 3.2 Data Preprocessing

Planetscope imagery was georeferenced to WGS-84 UTM Zone 37s, benefiting from its pre-orthorectified and radiometrically calibrated (TOA reflectance) state. This prevents misinterpretations from sensor artifacts (Bannari et al., 2016). For the PALSAR dataset, geometric correction, including alignment with ground control points and temporal offset estimation, ensured accurate geolocation and spatial consistency (JAXA (2012) PALSAR User's Guide). The WGS84/UTM Zone 37s projection was used. Additionally, all geological and topographical maps were meticulously spatially referenced and digitized to align with the remotely sensed data.

## 3.3 Lithological Mapping

This study utilized Support Vector Machine Learning classification (SVMLC) algorithm, to classify lithological rock units on Planetscope imagery (Maxwell et al., 2018; Shebl, A. & Cs'amer, 'A., 2021c.; Shirmard et al., 2022).

## 3.3.1 Enhancing Contrast (Saturation Stretch) Technique

Saturation stretch enhancement was applied to Planetscope images to improve visual clarity and emphasize key lithological features for training, using RGB composites from four-channel RGB-NIR data. Further processing methods are described in later sections. This technique enhances the visual appearance of the 3-band input image (R-4, G-3, and B-2) by increasing color saturation, making subtle lithological differences more discernible (Ijaajaane et al., 2025).

In this study, the saturation stretch technique was employed to enhance visual contrast among lithological units, particularly in regions exhibiting minimal spectral variation. Enhancing color saturation improved the visual separation of similar lithologies. Granitoid gneiss shows up in shades of light pink to pale brown, while Calc-Silicate can be found in dark green to black hues. Marbles typically appeared in light grey to bluish-white, and biotite gneiss ranges from brown to deep reddish tones. Lastly, magnetite-bearing granitoid gneiss presents itself in dark grey to bluish-black., aiding more accurate geological interpretation and lithological discrimination.

#### 3.3.2 Image Classification

The study area encompasses eleven primary information classes, which were systematically selected to ensure representative and spatially distributed training and testing samples. These classes were delineated using Planetscope imagery, informed by existing geological maps and visual image interpretation. A critical prerequisite to the classification process involves the identification of training samples, which act as reference inputs for the classification algorithm (Fig. 2).



# 3.3.3 Training and Evaluation Data

Modified geology map (Fig. 1a) guided the selection of training and evaluation data for eleven rock units, based on their texture and spatial distribution. A total of 3,564, 857 pixels (20.05% of the studied area) were identified as training dataset and used in SVM classifier. Additionally, 138 randomly positioned validation points served as the evaluation dataset (see Fig. 3). Sample distribution per unit is detailed in Table 3.

Table 3: Training and validation Lithological classifications samples

ID	Lithology Unit	Data (Training Pixels)	Data (Testing)
1	Quartz and Felspathic	142611	10
2	Crystalline Limestone	151649	5
3	Calc-Silicate	675589	5
4	Granitoid Gneisses	848851	50
5	Banded Pelitic	245928	12
6	Sillimanite Biotite	230953	7
7	Magnetite Granitoid	236182	5
8	Semi-Pelitic	713184	35
9	Lamprophyre	46150	1
10	Granite	448075	3
11	Hornblendites	47015	5

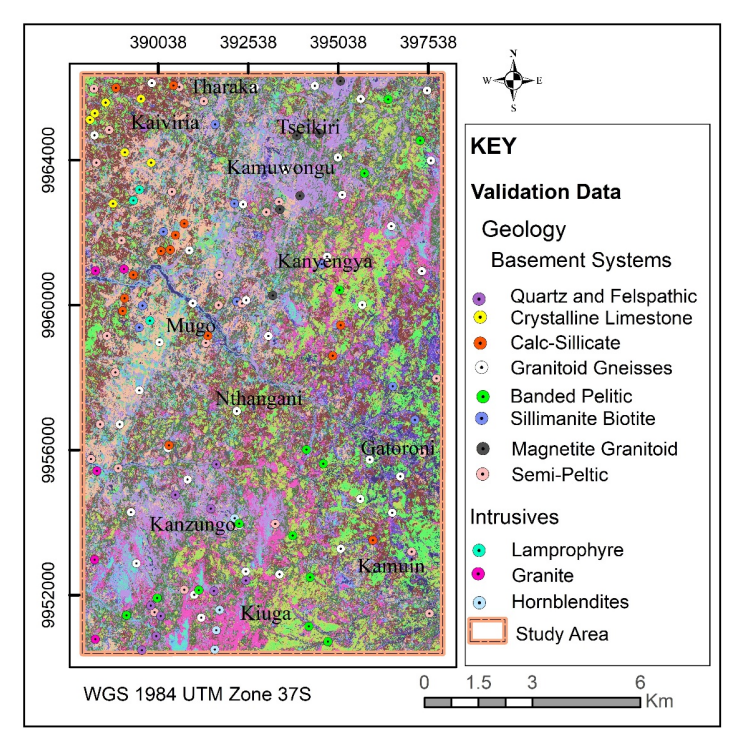


Fig. 3: Field Data Validation Map.

## 3.3.4 Lithological Classification

Support Vector Machine (SVM), a well-established algorithm in supervised machine learning based on statistical learning principles (Abdelkader et al., 2022), initially introduced by Vapnik and Chervonenkis in 1963. SVM



classification operates by identifying a boundary that best divides data points within a multi-dimensional feature domain. Ideal hyperplane is defined as the one that maximizes the margin between distinct classes (Wenyan Ge, 2020).

In the context of target detection, this process can be simplified to a binary classification problem. When applied in higher-dimensional spaces, SVM seeks the most suitable linear decision boundary that ensures maximal separation between the data classes (Bahrami et al., 2018). To handle the complexity of data distributed in high-dimensional spaces, a kernel function is employed, enabling the transformation of the input space into a more separable feature space. Radial basis functions (RBFs) exhibit greater kernel power compared to polynomial, linear, and radial kernels, leading to superior results in achieving better outcomes (Rimal et al., 2020). The (Equation 1) represents the radial basic function in SVM (Nurlina et al., 2021).

SVM, a widely adopted multivariate learning technique, is integrated into various software platforms. In this study, lithological mapping was conducted using a C++-based one-against-one SVM classifier. The kernel applied was the radial basis function with a regularization parameter of 100 and a gamma value of 0.091, corresponding to the Planetscope imagery pixel count (Ge et al., 2018).

## 3.4 Lineaments-Structural Mapping

Lineament extraction forms an integral part of geological mapping and mineral exploration, as mineralization often aligns with fracture zones (Zhang et al., 2022; Faruwa et al., 2021). In satellite imagery, lineaments appear as linear or slightly curved features, representing natural structures (e.g., faults, fractures, lithological contacts, drainage) or anthropogenic elements (e.g., roads, canals) (Bannari et al., 2016). Lineament delineation from remote sensing data is typically achieved through automatic or manual methods. Automatic extraction uses image-processing algorithms such as edge detection, while manual extraction relies on visual interpretation using enhanced imagery (Adiri et al., 2017; Ijaajaane et al., 2025). The choice between methods depends on study objectives and resource availability.

This study employed both automatic and manual lineament extraction to assess differences between the two approaches from Alos Palser DEM following the methodology proposed by (Choudhury et al., 2025). This approach aims to improve the extraction of tectonic-related lineaments from radar-based sensors. However, lineament identification can also be achieved using alternative data sources such as geomorphological features, morphometric indices, or optical satellite imageries (Zafaty et al., 2023). Manual lineament extraction entails three main stages: image enhancement, visual analysis, and digitization of linear features.

Manual extraction allows clear differentiation between natural and anthropogenic lineaments. This study focuses solely on tectonic features within rock outcrops, excluding drainage, roads, railways, and other human-made structures from the extraction process. In ArcGIS Pro, manual lineament extraction from ALOS PALSAR DEM eight shaded relief image employed using the cardinal angle directions at multiple azimuths (0°, 45°, 90°, 135°, 180°, 225°, 270°, and 315°) with a 45° altitude to enhance feature visibility (Fig. 4). The optimal contrast was achieved using azimuths 270° and 315°, which were selected for final extraction and rose diagram analysis. Shaded relief views depend on illumination angles. The LINE detection tool within PCI Geomatica Banff was employed with tailored criteria settings for the study area. The LINE module offers an optimized and mechanized solution for lineament recognition, supporting geological and geomorphological analyses. For optimal results, a filter radius (RADI) under 10 pixels and gradient-based edge threshold (GTHR) between 10-70 pixels are recommended (Choudhury et al., 2025).

Contour detection utilizes edge filtering to enhance pixel contrast. For effective lineament extraction, key parameters include a curve-length criterion (LTHR) set at 20 pixels to reduce noise, a line-fitting cutoff (FTHR) of 2-5 pixels for accurate approximation, and an angular difference threshold (ATHR) of 3–20° to accommodate natural orientation variations. The linkage distance criterion (DTHR), defining the peak gap allowed across polylines for connection, is set between 10–45 pixels to preserve structural continuity (N. Choudhury et al., 2025). These parameter ranges align with established best practices in automated lineament extraction (Awad, et al., 2022). Lineament extraction in PCI Geomatica was carried out through a series of predefined procedures applied to shaded relief ALOS PALSER DEM image, using software-specific parameters outlined in Table 4. Extracted lineaments were imported into ArcMap 10.8 for automating the splitting of combined lineaments into discrete segments on vertices. Lineament lengths and statistics were computed using the Calculate Geometry tool and cross-validated against 1:100,000-scale Tharaka-Kanzungo geology map (Fig. 1a). Data were then exported to GeoRose and Stereonet software, for the analysis and visualization of structural field records, including shear foliation, fold axes, and lineations. Rose and Stereonet diagrams and lineament density maps were generated to visualize structural orientations.



Orientations were measured in the field using a geological compass and subsequently plotted in Stereonet for structural interpretation. Non-structural features, such as contours, rivers, and cliffs, were excluded through visual interpretation, following established methodologies (Amraoui et al., 2025). A revised Litho-structural map was compiled by integrating remotely sensed result and previously reported geological and structural features with field observations. Field data were cross validated with remote sensing outputs and aligned with the principal orientations of major lineaments within the area.

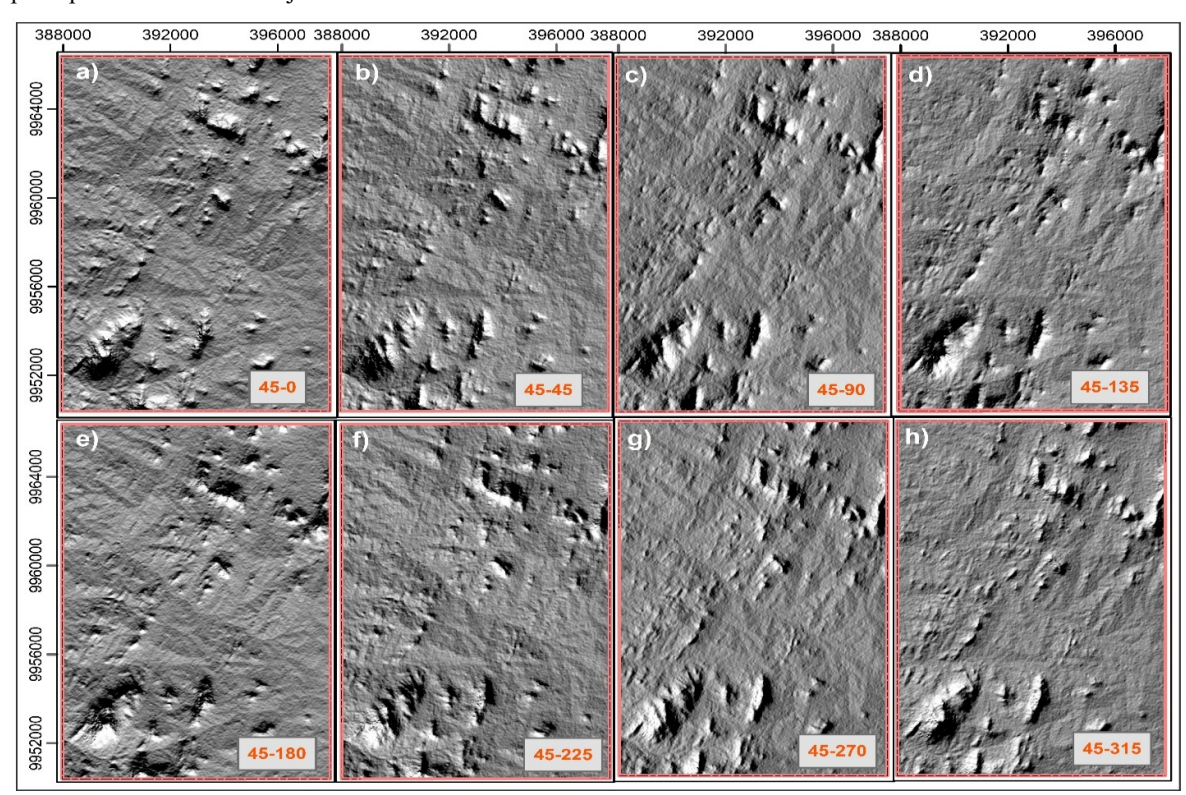


Fig. 4: Eight relief maps created using Alos Palser DEM 12.5m

Table 4: Criteria specifications used to delineate lineaments with the PCI Geomatica's LINE algorithm

Description	Criteria	Applied Values
Filter radius	RADI	10 pixel
Gradient-based edge threshold	GTHR	15
Curve-length criterion	LTHR	20 pixel
Line-fitting cutoff	FTHR	3 pixel
Angular variation limit	ATHR	15 degree
Linkage distance criterion	DTHR	10 pixel

## 3.5 Accuracy Evaluation and Field Validation

Classification accuracy was evaluated through producer accuracy (PA), user accuracy (UA), Kappa coefficient (K), and overall accuracy (OA), all derived from the confusion matrix (Lillesand et al., 2015; Congalton & Green, 2019). OA reflects the ratio of correctly categorized pixels, UA quantifies commission errors, and PA measures omission errors. Kappa coefficient quantifies consistency between the categorized map and reference data, accounting for chance. The range of Kappa values is 0 to 1, where values near 1 reflecting high classification confidence and those near 0 indicating significant uncertainty (Bachri et al 2019). Therefore, it is regarded as a more robust indicator of classification accuracy. Samples for training were conducted randomly,



informed by visual inspection of the geological map. Training samples were chosen through random selection based human-guided analysis of the geological map.

Fieldwork in the Tharaka-Kanzungo area validated Planetscope and ALOS PALSAR-derived maps through GPS surveying and georeferenced geological data. Litho-structural mapping captured key features, including faults, folds, mineralized zones, and shear structures within the Eastern Mozambique Mobile Belt. Accuracy assessment used ROIs from 1:100,000 maps stereonet and rose diagram analysis. Three new shear zones at Tharaka, Kanyengya near river Kalange and Kiuga were identified as potential extensions of the Tharaka-Kanzungo shear zone (Fig. 14) were identified and confirmed through remote sensing. The final map integrates field and remote data, offering a detailed geological and structural interpretation.

#### 4. Results

## 4.1 Lithological Mapping

In image analysis, color plays a key role in differentiating objects, enhancing image interpretation. To manage color effectively in satellite imagery, combining a minimum of three spectral bands (color composites) is essential. The study area is predominantly covered by lower to middle quartzite, marble, schist, biotite, and granitoid gneiss outcrops, whereas lamprophyre, limestone, granite, and hornblendite units are sparsely exposed in the northwestern, southeastern, and southern regions (Fig. 5).

We performed one distinct transformations on the RGB image (using bands 4, 3, and 2) to enhance the visual clarity of lithological facies in the study area. This transformation aimed to make it easier to identify different geological formations, and each one proved effective in bringing out specific geological units. Contrast enhancement using the 4-3-2 band combination revealed clear differentiation between the primary lithological units. Iron-rich rocks or weathered zones were displayed in brown-reddish tones, while fresh mafic or ultramafic rocks were identified by greenish-yellow hues. Silica-rich rocks appeared in bluish-cyan, and barren land are visible in grey-white colors (Fig. 5b).

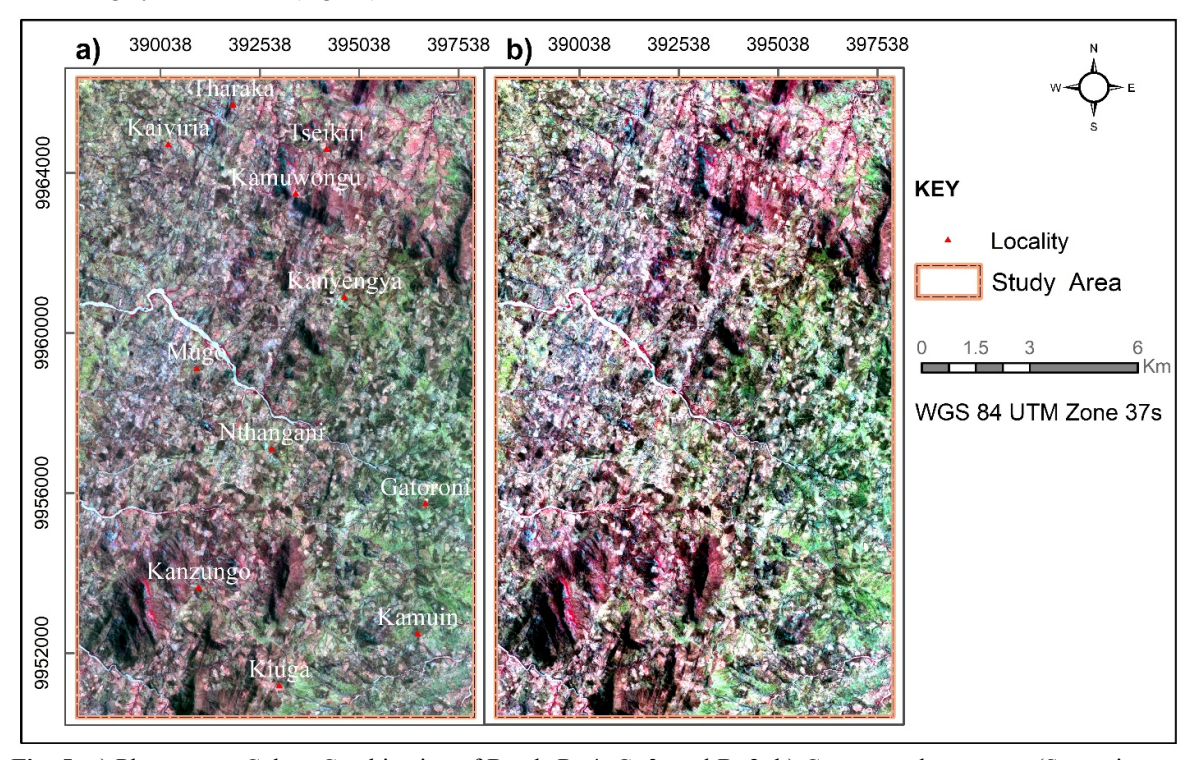


**Fig. 5:** a) Planetscope Colour Combination of Bands R=4, G=3, and B=2, b) Contrast enhancement (Saturation Stretch) of the color combination of Planetscope imagery bands R=4, G=3, B=2.

# 4.1.1 Lithological Classification

The SVM-based lithological map from Planetscope imagery, aiming to update the existing lithological map shows general agreement with the Tharaka-Kanzungo 1:100,000 geological map (Fig. 6), particularly for extensive facies. However, smaller units like hornblendite, lamprophyre and calc-sillicate formations appeared only faintly in the southern, western and northeastern section.



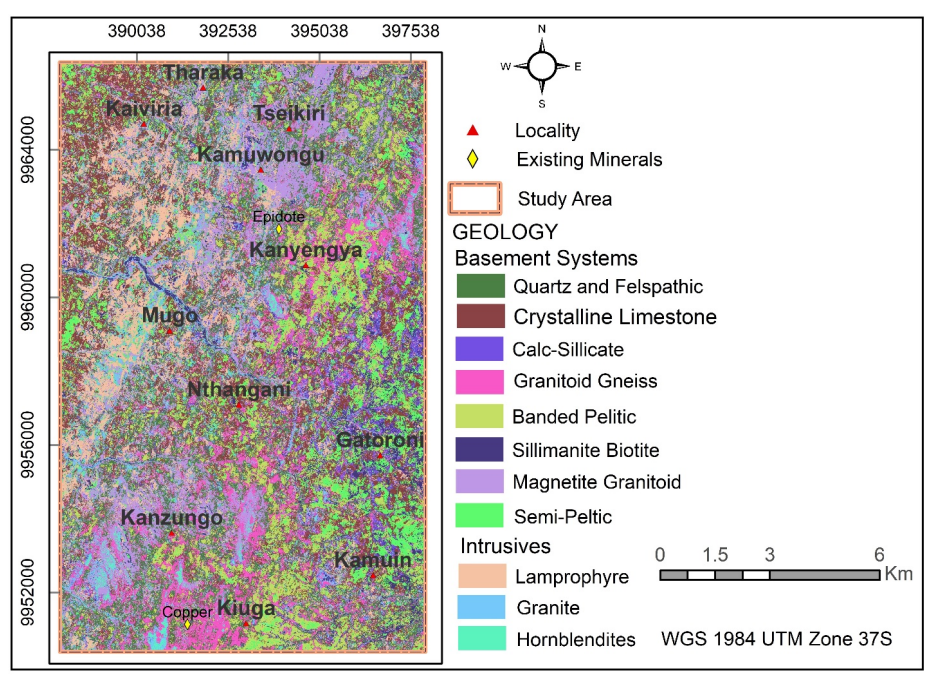


Fig. 6: Lithological Map produced using Support Vector Machine classifier on Planetscope imagery

# 4.1.2 Accuracy Evaluation and Validation

The lithological map's accuracy was assessed using independent validation samples, field observations, and reference to a geological map. To quantitatively assess classification performance, by SVM, a comparison was made with observed field features. Figure 7 highlights key locations used for visual verification. Figs. 9a–f present field photographs that highlight the dominant geological formations in the study area.

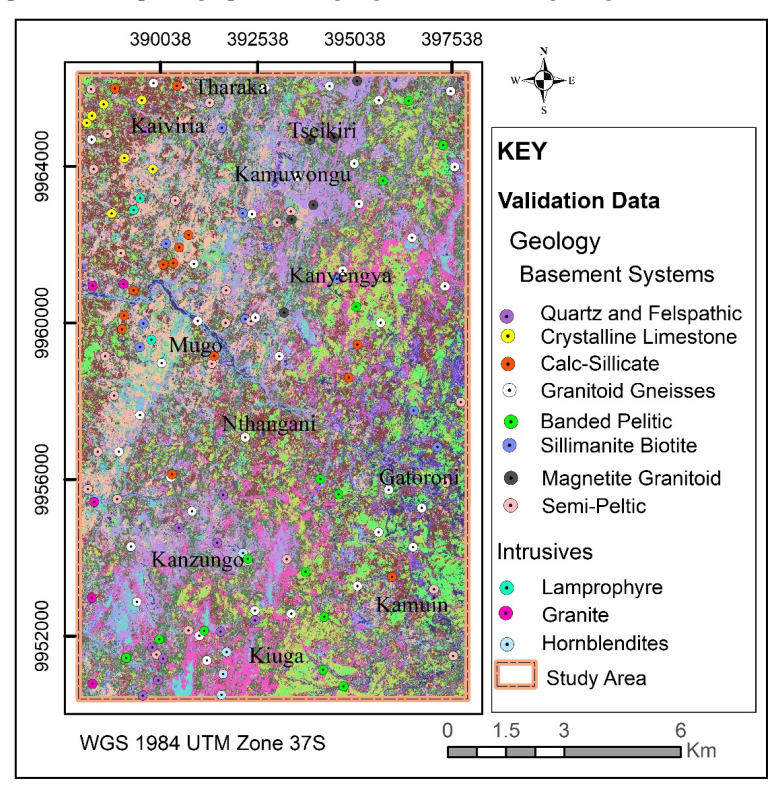


Fig. 7: Field Data - based Validation Map.



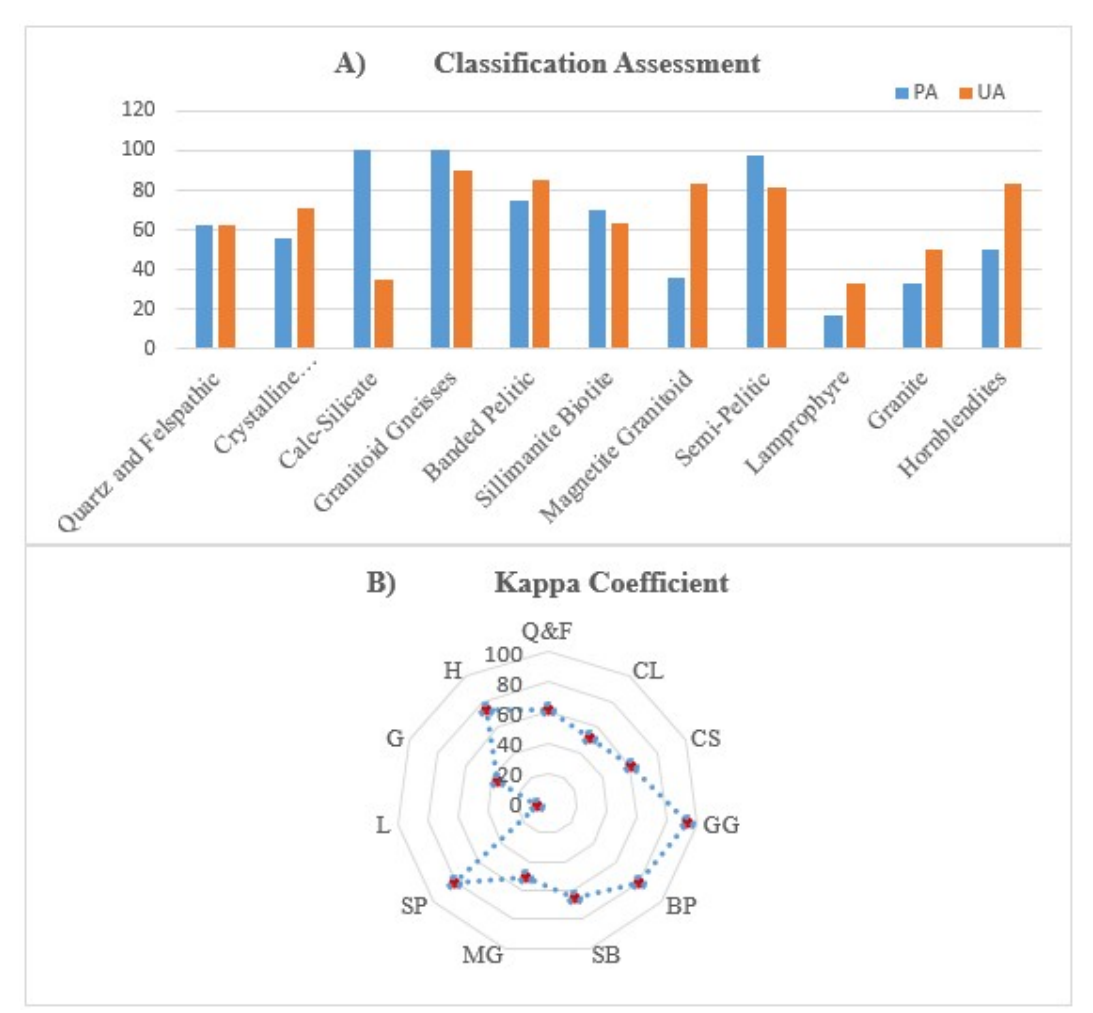
To quantitatively assess classification performance, 138 randomly selected ground-truth geological samples from the study area served as reference data for evaluation. Table 5 presents the OA, PA, UA, as well as Kappa for evaluating lithological classification via the SVM approach. SVM-based classification map achieved notably commendable accuracy, an achieved accuracy level of 76.24% alongside a Kappa statistic of 69.5%, indicated a pronounced agreement beyond random chance. This result clearly highlighted the superior capability of the SVM method in accurately identifying lithological units using Planetscope imagery (Fig. 6).

**Table 5:** Confusion matrix along with statistical metrics for Support Vector Machine (SVM) classification. Metrics for assessment included PA, UA, OA, and the Kappa (κ). **Key:** QF=Quartz and Felspathic, CL=Crystalline limestone, CS=Calc-silicate, GG=Granitoid gneisses, BP=Banded pelitic, SB=Sillimanite biotite, MG=Magnetite granitoid, SP= Semi-pelitic, L= Lamprophyre, G= Granite and H= Hornblendites.

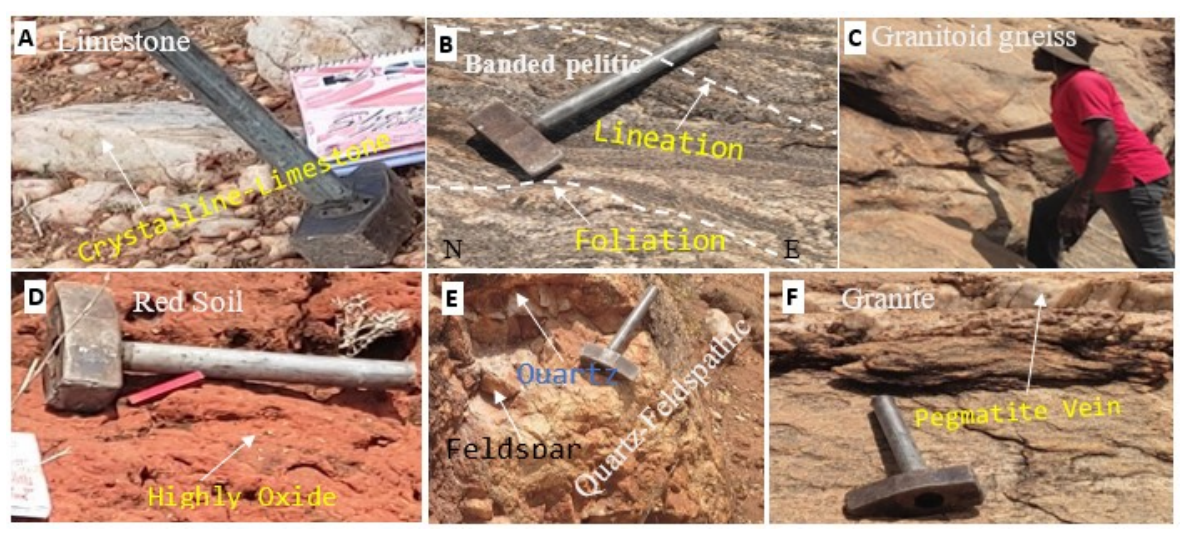
						]	Referen	ice						
Classification	Q&F	CL	CS	GG	BP	SB	MG	SP	L	G	Н	$\Sigma$ (User)	PA	UA
Q&F	10	0	0	0	1	1	1	0	0	2	1	16	62.5%	62.5%
CL	0	5	0	0	0	0	1	1	0	0	0	7	55.56%	71%
CS	1	1	5	0	1	0	2	0	1	2	1	14	100%	35%
GG	0	0	0	50	0	0	0	0	2	0	3	55	100%	90%
BP	0	1	0	0	12	0	0	0	0	1	0	14	75%	85%
SB	2	0	0	0	0	7	1	0	1	0	0	11	70%	63.64%
MG	0	0	0	0	1	0	5	0	0	0	0	6	35.71%	83.33%
SP	1	1	0	0	1	2	2	35	1	0	0	43	97.22%	81.40%
L	0	1	0	0	0	0	0	0	1	1	0	3	16.67%	33.33%
G	1	0	0	0	0	0	2	0	0	3	0	6	33.33%	50%
Н	1	0	0	0	0	0	0	0	0	0	5	6	50%	83.33%
Σ (Producer)	16	9	5	50	16	10	14	36	6	9	10	181	OA	76.24%
													K	69.72%

Figure 8a shows that the highest PA (>90%) was achieved for granitoid gneisses (GG), calc-silicate (CS), and semi-pelitic (SP), while the best UA (>80%) was observed for granitoid gneisses, banded pelitic (BP), magnetite granitoid (MG), hornblendite (H), and semi-pelitic. The granite (G) class had the lowest PA at 33.33%, indicating misclassification, partly due to random sampling, while lamprophyre (L) showed the lowest UA at 33.33%, highlight limitations in reliably identifying these specific lithologies. As shown in Figure 7b, granitoid gneisses (GG), semi-pelitic (SP), and banded pelitic (BP) exhibited the highest Kappa coefficients with 93.6%, 81.1%, and 80.5% respectively, whereas lamprophyre (L) recorded the lowest at 7.3%.





**Fig. 8:** Lithological classification accuracy for each class in the Planetscope data analyzed using the RBF SVM method, reporting: (a) PA and UA, and (b) Kappa coefficient for individual classes.



**Fig. 9:** Field photographs illustrating various rock units within the region. a) Crystalline-Limestone of the northern flank of Tharaka. b) Lineation and foliation layers of banded pelitic in Kanyengya. c) Granitoid gneiss dominating across the study area. d) Highly oxidized red soil in Ciampiu. e) Quartz-feldspathic in Kiuga and f) Pegmatite vein on granite rock in Ndiani.



#### 4.2 Lineaments-Structural Mapping

Shaded relief from ALOS PALSAR DEM enhances discontinuities for lineament mapping. To ensure objectivity, geological data were excluded during processing. Post-analysis, artificial lineaments are identified by overlaying roads, drainage, and geology, and subsequently removed. Table 6 and Figures 10-14 present results highlighting notable differences regarding lineament features among different datasets and techniques, underscoring the effectiveness for every method in extracting structural and geomorphological features.

#### 4.2.1 Manual and Automated Extraction

Manual delineation of lineaments from Alos Palser DEM imagery revealed structural trends and dimensional attributes. In total, 125 lineaments were mapped (Fig. 10a), varying from 157 m to 3049 m, with a mean value of 1031 m. Rose diagram results reveal a prevailing NE-SW (around 45°-90°) and minor E-W orientation, aligning with surface patterns observed in the remote data (Fig. 12a).

Automatic lineament extraction produced a substantially greater number of lineaments, totaling 334 features (Fig. 10b), ranging from 1562 m to 250 m and averaging around 363 m in length. Rose diagram results show a primary NNW-SSE (around 135°) and minor NW-SE trend, Fig. 12b), indicating a key structural alignment in that direction captured by the radar data.

Table 6: Statistical summary of Manual and automatic lineaments extracted from Alos Palser DEM data.

Type of Data	Number of	Total length of	Max (m)	Min (m)	Mean (m)
	Lineaments	Lineaments			
Alos Palser DEM	125	128870	3049	157	1031
(Manual)					
Alos Palser DEM	334	121323	1562	250	363
(Automatic)					

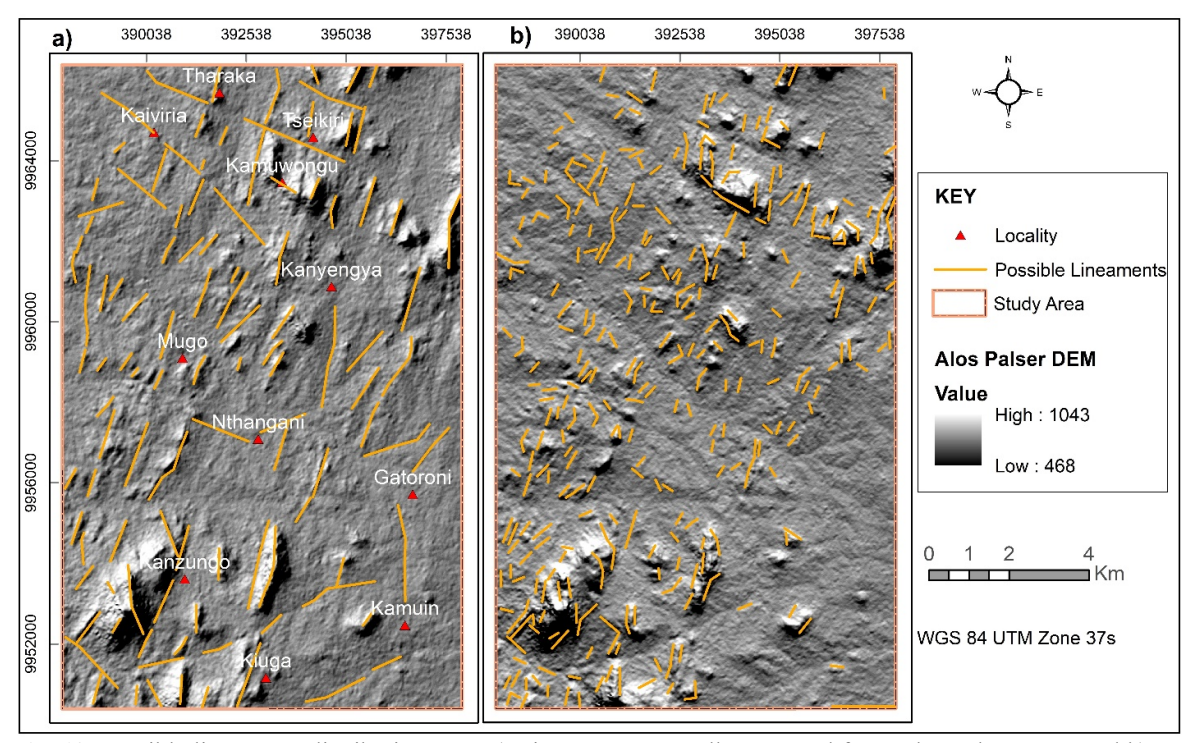


**Fig. 10:** Possible lineaments distribution map: a) Lineaments manually extracted from Alos Palser DEM and b) Lineaments automatically derived from Alos Palser DEM data.

## 4.2.2 Lineament Distribution Density Map (LDDM)

The research area exhibits generally low lineament distribution density (Fig. 11), with the highest concentrations in mountainous regions. Moderate densities border these, while the lowest values occur in populated troughs and lowlands, with isolated moderate density zones. Draping the geological map with the lineament distribution density map reveals a clear correlation, where high densities align with intensely fractured zones. The southwestern high-density area corresponds to the NE-SW and NW-SE Kanzungo area, fault corridor occupying



the study area's core. The southeastern section of the research area, covering the Gatoroni and Kamuin shows low density of lineaments due to moderate urbanization. However, small enclaves exhibit high densities. Lineament variability is primarily influenced by geology and rock outcrops.

Lineament density analysis highlights notable variations across the Alos Palser DEM and extraction methods, especially in distribution and concentration. Manual yields a dispersed and less structured LDD pattern, with a peak of 3.72 km/km² (Fig. 11a). In contrast, automated exhibits a higher and stronger focused LDD, a modest increase to 4.63 km/km² (Fig. 11b). These results, despite varying methods, indicate comparable structural influences.

The highest lineament densities are concentrated within the western, northern, southwestern, northwestern, and central sector of the study region, regardless of the extraction method, while the southeastern region shows the lowest values. The Alos Palser DEM data proves effective for lineament analysis. Automatic extraction yields the highest lineament count and density, supporting its value in structural mapping. Manual analysis emphasizes trends oriented NE–SW and NW–SE, contrasting automated NNW–SSE results, showing complementary structural insights (Fig. 11).

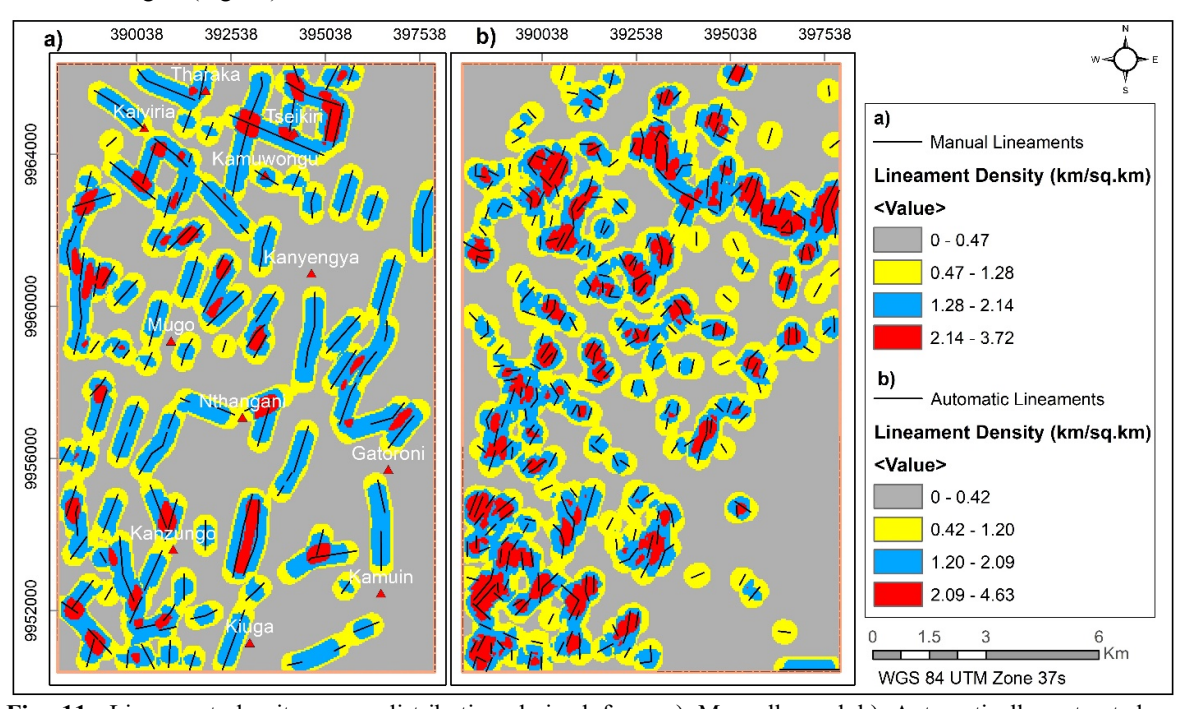


Fig. 11: Lineament density maps distribution derived from a) Manually and b) Automatically extracted lineaments using Alos Palser DEM

## 4.2.3 Orientations of Lineament

To examine azimuthal variability and dominant structural orientations, rose diagrams were utilized. This study generated diagrams for lineaments obtained from ALOS PALSAR DEM using automatic and manual extraction techniques (Fig. 11). Automatically delineated lineaments show a dominant NNW-SSE (around 135°) and minor NW-SE orientation, while manual extraction reveals an NE-SW (around 45°-90°). The rose diagrams (Fig. 12a-b) clearly illustrate dominant structural alignments of N-S, NNW-SSE, and NE-SW complemented by NW-SE being the most prominent. Also, emphasize the complementary strengths of automation in detecting geological structures.

Stereographic projections and lineation of field measurements helped us evaluate structural directions, revealing significant aspects of the area's deformation processes. The general trend of the structures follows the Northeast-Southwest and Northwest-Southeast (Fig. 12c-d), with minor north south (N-S) trends. These alignments suggest structural controls on fluid flow and mineralization, with stereonets confirming a complex fault system likely influenced by regional tectonic stresses (Fig. 12c-d).



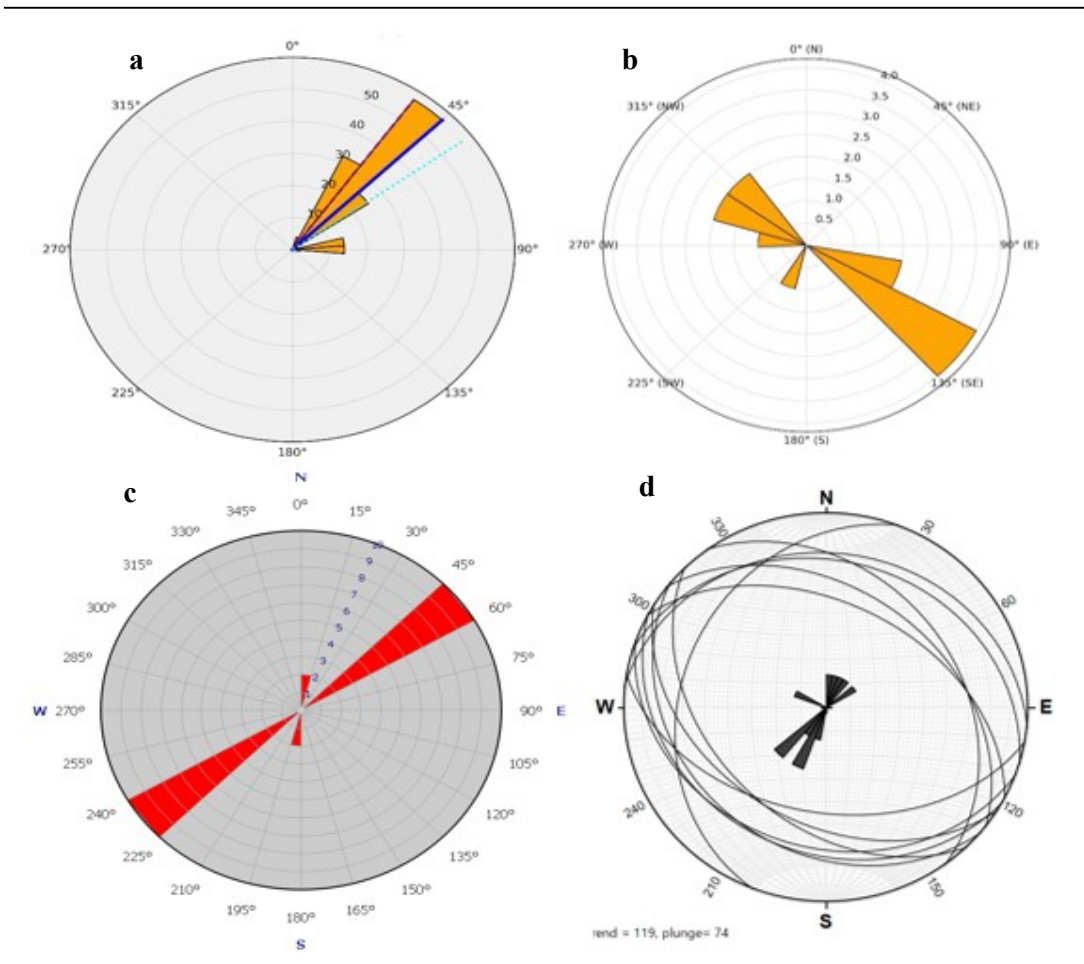


Figure 12: Rose and stereonet diagrams showing linear-structural trend from Alos Palser DEM: a-b) Manual and automatic remote extraction; c-d) Field based lineation and stereographic measurement

## 4.3 Field Validation

Field checks, supported by existing literature (Dodson, 1955; Crowther, 1957; Githenya et. al., 2021), confirmed faults, folds, and joints, particularly in Tharaka, Kiuga, Ndiani, Kanyengya and Kamwerini. Figure 13 shows selected validation points, representing outcrop-scale fault and mineralization observations across the study area. Field observations confirmed a strong spatial association among copper, iron-rich zones, quartz anomalies and fault structures zones near Kanzungo, Ciampiu, and Kanyengya distributed across the southwestern, central, and northern portions of the study region (Fig. 14a-n). Additionally, copper enrichment correlates well with argillic and silica alteration zones. Field analyses further validate the presence of new copper prospects in western and central portion of the region (Fig. 14g)



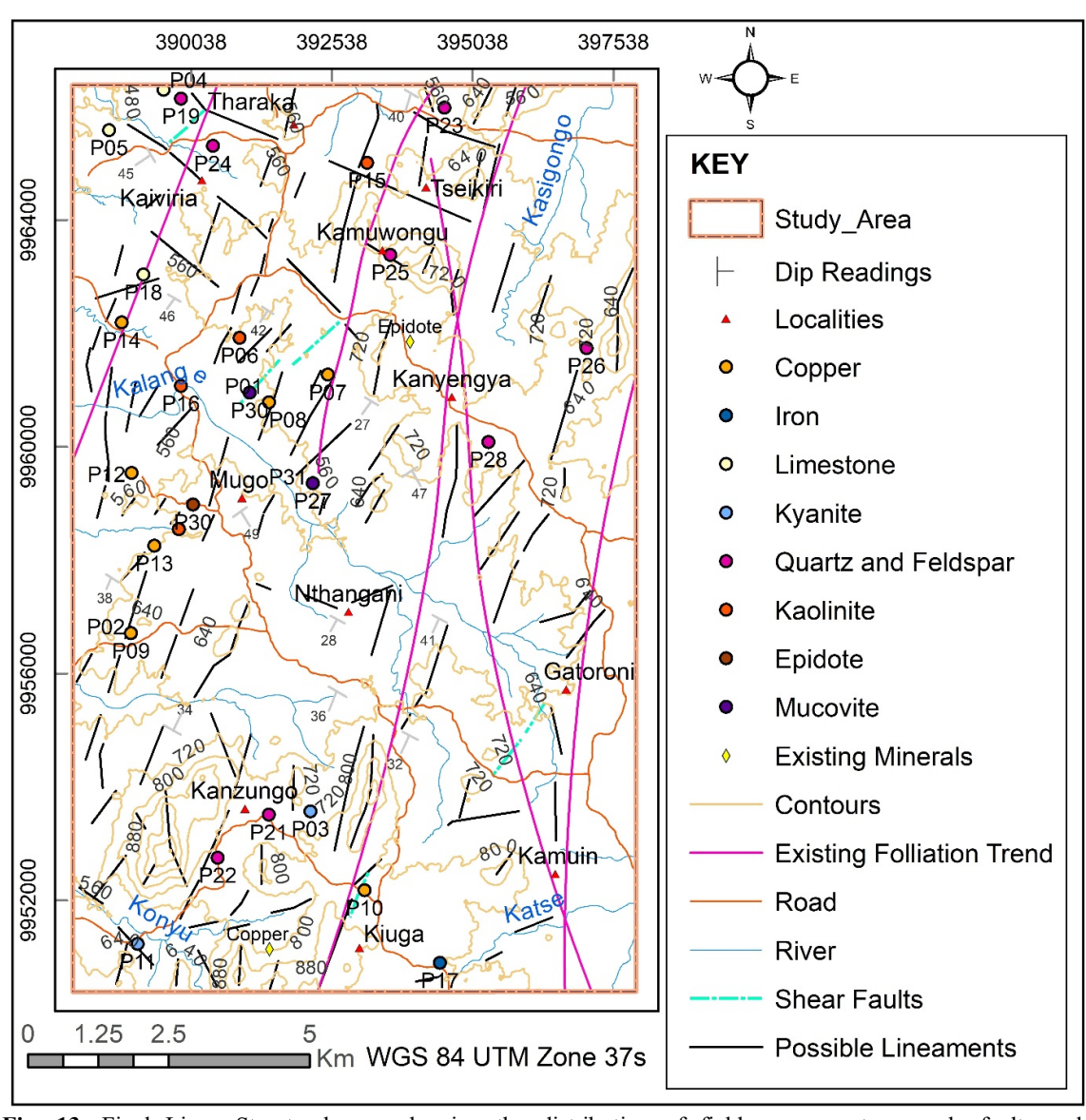


Fig. 13: Final Linear-Structural map showing the distribution of field survey outcrop-scale faults and mineralization points (positions) across the study area.





Fig. 14: a) Sericite alteration showing white mica, b) Silicification prominent in faulted zones (Kiuga), c) Argillic Zone widespread, linked to clay mineral, d) Heavy Mineral Sands and magnetite rich iron mineral (Ndiani & Mukuruni area) in River Keera, e-f) Quartz and feldspar mineral on granitoid gneiss, g) Fault-related copper mineralization (malachite and azurite), h) Crystalline Limestone, i-j) Shear joints and Strike-slip faults, k) Quartz and Feldspar vein, l) Biotite gneiss showing foliation and lineation trend and mineral banding, n) Strained mylonites.

#### 5. Discussion

Machine learning Models (MLMs) are increasingly valuable within remote sensing for geological mapping, addressing cost, complexity challenges often associated with hyperspectral and multispectral imagery (Bachri et al., 2020). This study assessed SVM's performance for lithological classification in arid and semi-arid land (ASAL), proving reliable for most rock units, including granitoid gneiss and pelitic schists, though lamprophyre detection was limited. Planetscope imagery significantly enhanced textural detail, aiding classification.



While SVM-based automatic classification generally outperformed the existing geological map in accuracy metrics, its detection of hornblendite veins remained limited, showing lower agreement for hornblendite and sillimanite-biotite units (Fig. 6). These limitations are attributed to factors like differential weathering, mineral composition variability, and image resolution. Overall, the applied method offers an efficient and rapid alternative to traditional field mapping for generating and updating lithological maps in remote regions, reducing time and resource demands.

Linear-structural analysis, leveraging ALOS PALSAR DEM and remote sensing data, gave us important details about the study area's tectonic evolution consistent with findings by (Dodson, 1955; Crowther, 1957; Nyamai et al., 1993). Manual lineament extraction, prioritized for its interpretive reliability, revealed a dominant NE–SW trend, whereas automatic methods yielded more numerous, shorter features trending NNW–SSE. Field measurements confirmed dominant NE-oriented shear foliations, indicative of compressional stress, with good correspondence between these and major remote sensing trends. ALOS PALSAR DEM effectively captured key Linear-structural features and fault systems controlling mineralization, highlighting deformation zones. Despite inaccessibility limiting field verification of some shear zones, remote sensing successfully revealed structurally significant lineaments, addressing a key literature gap by producing a detailed structural map of the EMMB.

#### 6. Conclusions

This study significantly enhanced litho-structural mapping in Tharaka-Kanzungo by integrating high-resolution PlanetScope imagery and ALOS PALSAR DEM with field data. SVM-based classification achieved 76% accuracy (Kappa 0.7), while automated lineament extraction revealed dominant Northeast–Southwest, NNW–SSE, North–South, and Northwest–Southeast trends. These structural features, including north-dipping shear foliations, align with key mineral-related fault zones and reflect an N–S stress regime from the Eastern Mozambique Mobile Belt, effectively channeling vein-hosted copper, iron, silica, and kaolinite mineralization (Dodson, 1955; Crowther, 1957; Githenya et. al., 2021). Field investigations further confirmed unmapped minerals and consistent sheared rock exposures. This research highlights the complementary strengths of remote sensing datasets and the necessity of cross-validation for accurate mapping and mineral exploration in complex, inaccessible terrains. Future work should integrate LiDAR and hyperspectral data for enhanced interpretation and geophysical survey.

**Acknowledgment:** We acknowledge the USGS, Alaska Facility Services, and NASA for providing ASTER, Sentinel-2A, PlanetScope, and ALOS/PALSAR DEM data. We thank the Kenya State Dpt. of Mining for laboratory analysis and the Department of Geology and Meteorology, South Eastern Kenya University for its support in supplying field equipment.

## References

- Abdelkader et al. (2022). Effective delineation of rare metal-bearing granites from remote sensing data using machine learning methods: A case study from the Umm Naggat Area, Central Eastern Desert, Egypt. Retrieved from doi.org/10.1016/j.oregeorev.2022.105184
- Adiri, Z., Harti, E., A., Jellouli, A., & Lhissou. (2017). Comparison of Landsat-8, ASTER and Sentinel 1 satellite remote sensing data in automatic lineaments extraction: A case study of Sidi Flah-Bouskour inlier, Moroccan Anti Atlas. *Advances in Space Research*, 60(11), 2355–2367. doi:10.1016/j.asr.2017.09.006
- Amraoui, T., Ibouh, H., Farah, A., Bammou, Y., & Shebl, A. (2025). Remote sensing mapping of structural and hydrothermal alteration in the mougueur inlier, Eastern high atlas, Morocco. Morocco: Natureportfolio. doi:10.1038/s41598-025-99402-0
- Awad, H. A., El-Leil, I., Kamel, M., Tolba, A., Nastavkin, A., & El-Wardany, R. (2022). Geological features identified from field observations and Remote Sensing data. geodynamics & tectonophysics, 13(3), 0646. doi:10.5800/GT-2022-13-3-0646
- Bachri, I., Hakdaoui, M., Raji, M., & Benbouziane, A. (2020). Geological mapping using Random Forests applied to Remote Sensing data: a demonstration study from Msaidira-Souk Al Had, Sidi Ifni inlier (Western Anti-Atlas, Morocco). 2020 IEEE International conference of Moroccan Geomatics (Morgeo) (pp. 1-5). Morocco: IEEE.
- Bahrami, Y., Hassan, H., & Maghsoudi, A. (2021). Investigating the capabilities of multispectral remote sensors data to mapalteration zones in the Abhar area, NW Iran. *GEOSYSTEM ENGINEERING*, 24(1), 18–30. Retrieved from https://doi.org/10.1080/12269328.2018.1557083
- Bannari et al. (2016). PALSAR-FBS L-HH Mode and Landsat-TM Data Fusion for Geological Mapping. . *Advances in Remote Sensing*, 5, 246-268, doi:doi.org/10.4236/ars.2016.54020
- Cardoso-Fernandes, J., Teodoro, A., Lima, A., & Roda-Robles, E. (2020). Semi-Automatization of Support Vector Machines to Map Lithium (Li) Bearing Pegmatites. *Remote Sensing*, 12(2319). Retrieved from https://doi.org/10.3390/rs12142319



- Chepchumba, M. C., Raude, J. M., & Sang, J. K. (2019). Geospatial delineation and mapping of groundwater potential in Embu County, Kenya. *Acque Sotterranee Italian Journal of Groundwater*, 8(2), 39–51. doi:10.7343/as-2019-369
- Choudhury, N., Mitra, A. K., Nath, B., & Lindsay, M. D. (2025). Lineament extraction and structural mapping using Landsat-9 OLI and Sentinel-1 SAR data in the Proterozoic North Singhbhum Mobile Belt, Eastern India. *Geosystems and Geoenvironment*, 4(3), 100392. doi:10.1016/j.geogeo.2025.100392
- Congalton, R. G., & Green, K. (2019). Assessing the Accuracy of Remotely Sensed Data Principles and Practices, Third Edition. 6000 Broken Sound Parkway NW, Suite 300 Boca Raton, FL 33487-2742: Taylor and Francis Group. Retrieved from http://www.crcpress.com
- Crowther, A. F. (1957). Geology of the Mwingi Area, North Kitui" Report. Geol. Surv. Kenya (in preparation). Dodson, R. G. (1955). Geology of the North Kitui Area. Geol. Surv. Kenya.
- Faruwa et al. (2021). Aeromagnetic and remote sensing characterization of structural elements influencing iron ore deposits and other mineralization in Kabba, southwestern Nigeria. *Adv. Space Res.*, 68(8), 3302-3313. doi:doi.org/10.1016/j.asr.2021.06.024.
- Ge Wenyan, Cheng, Q., Tang, Y., Jing, L., & Gao, C. (2018). Lithological Classification Using Sentinel-2A Data in the Shibanjing Ophiolite Complex in Inner Mongolia, China. *10*(4), 638. doi:10.3390/rs10040638
- Githenya et. al. (2021). Integration of Remote Sensing and Geological Mapping for Economic Mineralization Mapping in Mwitika-Makongo Area, Kitui County. *J Remote Sens GIS.*, 10, 281.
- Githenya, L. K., Kariuki, P. C., & Waswa, A. K. (2019). Application of Remote Sensing in Mapping Hydrothermal Alteration Zones and Geological Structures as Areas of Economic Mineralization in Mwitika-Makongo Area, SE Kenya. *Environment and Earth Science*. Retrieved from https://doi.org/10.7176/JEES/9-11-03
- Hu, B., Xua, Y., Wana, B., Wua, X., & Yic, G. (2018). Hydrothermally altered mineral mapping using synthetic application of Sentinel-2A MSI, ASTER and Hyperion data in the Duolong area, Tibetan Plateau, China. *Ore Geology Reviews*, 101, 384–397. Retrieved from https://doi.org/10.1016/j.oregeorev.2018.07.017
- Ijaajaane, A., Abdelhak and Si Mhamdi, Hicham and Tariq, & Aqil and Ali. (2025). Remote Sensing Contributions to Lithostructural Mapping Using Sentinel 2A Data: A Case Study of the Errachidia Area (Central High Atlas, Morocco). *Iraqi Geological Journal*, 58(1C). doi:10.46717/igj.58.1C.11ms-2025-3-26
- Japan Space Systems (2012) PALSAR User's Guide. 2nd Edition. https://www.scribd.com/document/208847444/Palsar-User-Guide
- Karuku, W. D. (2008). Characterization of copper minerals in kanzugo area of the Mozambique mobile belt, thesis. University of Nairobi.
- Kiptarus, J., Muumbo, A., Makokha, A., & Kimutai, S. (2015). Characterization of Selected Mineral Ores in the Eastern Zone of Kenya: Case Study of Mwingi North Constituency in Kitui County. *Mining Engineering and Mineral Processing*, 4(1), 8-17. doi:10.5923/j.mining.20150401.02
- Kugeria, P. M., & Njoroge, P. W. (2022). Analysis of Copper Deposits in Maragwa Location in Tharaka Nithi County – Kenya. American Journal of Materials Science, 12 (1), 18-24. doi:DOI: 10.5923/j.materials.20221201.03
- Lillesand, T., Kiefer, R., & Chipman, J. (2015). Remote Sensing and Image Interpretation. In T. Lillesand. John Wiley & Sons. Retrieved from https://www.wiley.com/en-us/Remote+Sensing+and+Image+Interpretation%2C+7th+Edition-p-9781118343289
- Maarifa et al. (2024). Mapping of surface hydrothermal mineral alterations and geological structures related to geothermal systems in the Songwe region, SW Tanzania. doi:10.1080/12269328.2023.2299481
- Maghsoudi, F., & Nader Fathianpour. (2016). Application of AHP method in Copper potential mapping, Case study: Central Kerman Metallogenic arc. 4th International Mine and Mining Industries Congress and Expo and 6th Iranian Mining Engineering Conference. Tehran: IRAN MINE HOUSE. Retrieved March 2024
- Maxwell, A., Warner, T., & Fang, F. (2018). Implementation of machine-learning classification in remote sensing: An applied review. *International Journal of Remote Sensing*, 39, 2784–2817.
- Nurlina, Syarifuddin, K., Ahmad, K., & Wahyuni, I. (2021). Comparison of maximum likelihood and support vector machine classifiers for land use/land cover mapping using multitemporal imagery. *Academic Research International*, 12 (1), 2223-9944. Retrieved from www.journals.savap.org.pk
- Nyamai, C. (1999). Crustal Evolution of the Neoproterozoic Mozambique Belt Rocks in Matuu-Masinga Area, Central Kenya: An Implication to their Tectonic Setting and Potential Mineralization.



- Nyamai, C., Mathu, E., & Ngecu, W. (1993). A review of the geology of the Mozambique Belt in Kenya. Proceedings of the 9th International Geological Conference of the Geological Society of Africa - Regional Trends in African Geology, (pp. 334-347). Accra. Ghana.
- Ombiro, et al. (2021). Application of remote sensing in mapping hydrothermally altered zones in a highly vegetative area A case study of Lolgorien, Narok County, Kenya. *Indian Journal of Science and Technology*, 14(9), 810-825. Retrieved from https://doi.org/10.17485/IJST/v14i9.68
- PCI-Geomatics (2015) Using PCI Software. Richmond Hill, ON, Canada. http://www.pcigeomatics.com/Planet, L. (2018). Planet Imagery Product Specifications.
- Planet, T. (2024). Planet Imagery Product Specifications. *Planet Lab*. Retrieved from https://assets.planet.com/docs/combined-imagery-product-spec-final
- Pour, A. B., & Hashim, M. (2014). Integrating PALSAR and ASTER data for mineral deposits exploration in tropical environments: a case study from Central Belt, Peninsular Malaysia. *International Journal of Image and Data Fusion*, 6(2), 170-188. Retrieved from https://doi.org/10.1080/19479832.2014.985619
- Rimal, B., Rijal, S., & Kunwar, R. (2020). Comparing Support Vector Machines and Maximum Likelihood Classifiers for Mapping of Urbanization. *Journal of the Indian Society of Remote Sensing*, 48(1), 71–79. Retrieved from https://doi.org/10.1007/s12524-019-01056-9
- Roy, D. P., Huang, H., Houborg, R., & Martins, V. S. (2021). A global analysis of the temporal availability of PlanetScope high spatial resolution multi-spectral imagery. *Remote Sensing of Environment*, 264, 112586. Retrieved from https://doi.org/10.1016/j.rse.2021.112586
- Shebl, A. & Cs'amer, 'A. (2021). Stacked vector multi-source lithologic classification utilizing Machine Learning Algorithms: Data potentiality and dimensionality monitoring. *Remote Sens. Appl.: Soc. Environ.*, 24.
- Shirmard, H., Ehsan Farahbakhsh, R. Dietmar Müller, & Rohitash Chandra. (2022). A review of machine learning in processing remote sensing data for mineral exploration. *ESEVIER*, 268, January 2022, 112750. Retrieved from https://doi.org/10.1016/j.rse.2021.112750
- Waswa, A. K. M., Nyamai, C. M., Mathu, E. & Ichangi, W. D. (2015). Integration of Geological Mapping and Remote Sensed Studies for the Discovery of Iron–Ore Mineralization in Mutomo–Ikutha Area, SE Kenya. *Universal Journal of Geoscience*, 3(2), 39.
- Wenyan et al., (2020). Assessment of the Capability of Sentinel-2 Imagery for Iron-Bearing Minerals Mapping: A Case Study in the Cuprite Area, Nevada.
- Zafaty et al. (2023). Integrated remote sensing data and field investigations for geological mapping and structural analysis. The case of SW Tichoukt ridge (Middle Atlas, Morocco).
- Zhang et al. (2022). Ore-controlling structures of sandstone-hosted uranium deposit in the southwestern Ordos Basin: revealed from seismic and gravity data. . *Ore Geol. Rev.*, 140, 590. doi:doi.org/10.1016/j.oregeorev.2021.104590.
- Zhang, Q., Guo, Z., Liu, L., Mei, J., & Wang, L. (2025). Lithological classification using SDGSAT-1 TIS data and three-dimensional spectral feature space model. *International Journal of Digital Earth*, 18(1), 2467983. doi:10.1080/17538947.2025.2467983